IEEE Access
Multidisciplinary | Rapid Review | Open Access Journal

Received February 21, 2021, accepted March 4, 2021, date of publication March 9, 2021, date of current version March 15, 2021.

Digital Object Identifier 10.1109/ACCESS.2021.3064605

Beamforming Using Uniform Spherical Arrays: Array Construction, Beam Characteristics, and Multi-Rank Transmission

WONJAE RYOO, (Student Member, IEEE), AND WONJIN SUNG, (Member, IEEE)
Department of Electronic Engineering, Sogang University, Seoul 04107, South Korea

Corresponding author: Wonjin Sung (wsung@sogang.ac.kr)

This work was supported in part by the National Research Foundation (NRF) of Korea, Ministry of Science, ICT and Future Planning (MSIP) under Grant NRF-2020R1A2C1004135, and in part by LG Electronics.

ABSTRACT 5G new radio (NR) provides features such as enhanced mobile broadband (eMBB) services and massive machine-type communications (mMTC). Multiple-input multiple-output (MIMO) transmission is an essential technique to enable these features, using antenna arrays with a sufficient number of elements to generate accurate and high-gain beams to desired user locations. In newer services, various forms of mobile devices are expected to appear in diverse locations, and beamforming need to accommodate such directional diversification. However, utilization of existing array structures has a limitation in transmitting signals to arbitrary receiver positions in the three-dimensional space. Therefore, a new type of array capable of forming accurate beams in isotropic fashion is desired, and the corresponding transmission strategies need to be identified. In this paper, the construction and utilization of the three-dimensional uniform spherical array (USA) are investigated. Beamforming vectors and the basis codebook for such arrays are defined, and characteristics of the generated beams are analyzed via comparison to the beams produced by conventional arrays. Array parameters to minimize the inter-beam interference are determined, and multiuser transmission performance is evaluated using the proper configuration of the array. We also apply the radiation pattern to the antenna elements to present the sum-rate performance in practical settings.

INDEX TERMS 5G NR, massive MIMO, beamforming, codebook, millimeter-wave, spherical array.

I. INTRODUCTION

5G new radio (NR) can achieve the maximum data rate up to 20 Gbps by utilizing the millimeter-wave (mmWave) spectrum and large-scale arrays for massive multiple-input multiple-output (MIMO) transmission [1]. With the development of services that require increased data rates such as super high-definition (SHD) video and virtual reality (VR), next-generation wireless systems will heavily rely on higher frequency bands including the mmWave spectrum [2], [3]. To compensate for the severe power attenuation experienced at these frequency bands, channel characteristics and high-gain beamforming strategies over the line-of-sight (LoS) channel have been intensively studied [4]–[7].

Wireless connectivity requirements for internet-of-things (IoT) and massive machine-type communications (mMTC) not only increase the number of mobile terminals connected to the network, but necessitate the support for the diversification of user locations. An increasing demand for vehicle-to-everything (V2X) communications also requires radio access and beam management (BM) techniques to handle highly mobile users in various locations [8], [9]. The coverage for radio access is now broadened to all directions in the entire three-dimensional (3D) space with aerial applications including drone mobiles and unmanned aerial vehicle (UAV) base stations [10]–[12]. It is very clear that aforementioned types of transceivers will benefit from antenna arrays capable of forming accurate beams and providing a seamless coverage in isotropic fashion.

The coverage of generated beams is directly related to the shape of antenna arrays. In [13], possible usages of planar, circular, and hexagonal arrays for mmWave transmission and the corresponding beam patterns are discussed. Currently, the most widely adopted array model is the uniform planar array (UPA), which is the two-dimensional extension of the uniform linear array (ULA). Accordingly, the 3GPP

The associate editor coordinating the review of this manuscript and approving it for publication was Wence Zhang.

standard specifies the beamforming vectors and codebooks based on UPAs [14], [15]. Extensive research results exist in the related areas, including the beam generation with variations in vertical user positioning [16], [17], multi-rank beam transmission over the 3D spatial channel model [18], [19], and related hybrid beamforming [20], [21]. The array configuration extended to multiple panels has been studied in [22], [23]. Beamforming in 3GPP requires the transmission of reference signals and the feedback of the precoder matrix indicator (PMI) and channel quality indicator (CQI) [15], [24]. For MIMO systems using a large-scale array, a significant increase in complexity and signaling overhead is expected for this process. Instead, the channel is estimated by using uplink training assuming the time-division duplexing (TDD) operation [25]. For channels which can be determined by the user location, only a few parameters suffice to estimate the channel and the Fourier decomposing method of the training signal can be applied [26]. Investigation results in [25] and [26] emphasize the advantage of applying the pilot technique to antenna array at the base stations or access points for obtaining the MIMO channel matrix. Dynamic pilot scheduling scheme has also been applied to 5G ultra-dense networks [27]. In addition to the aforementioned schemes, design and utilization of the beam codebooks have been studied for the effective coverage of the 5G MIMO channels [28], [29]. More recently, directional beamforming and beam management strategies are applied to millimeter-wave channels for efficient data transmission over the link exhibiting a significant pathloss [30]–[32].

Although UPAs efficiently control beam directions in both azimuth and zenith angles, the beam gain decreases as the direction deviates from the array boresight and the effective coverage is restricted over a limited range of angles. In order to provide a uniform received power level over the entire azimuthal plane, beamforming utilizing uniform circular array (UCA) and transformation methods to convert existing codebooks for transmission using such arrays have been proposed [33]–[35]. Recent efforts to apply UCAs to mmWave LoS channels and hybrid beamforming can be found in [36]–[38], and the array gain of UCAs mounted on a cylinder is analyzed in [39]. Despite its enhanced capability to form uniform beams over the horizontal space, the UCA still exhibits limitations to cover users with wide vertical mobility.

Small cells in 5G systems may include radio units installed on an indoor ceiling to perform vertical downtilt transmission, on a street lamp post to support vehicular users, and on a building rooftop to communicate with aerial mobiles. To accommodate such transmission scenarios, a new type of antenna array is desired, and an ultimate form of the array structure for all-directional beamforming is based on a sphere. In fact, antenna structures based on spherical geodesic domes are designed and constructed for satellite communications to provide reliable communication links to geostationary satellites [40], [41], and wave propagation analyses for spherical audio speakers can be found in [42], [43]. Design trade-offs of spherical arrays are investigated in [44], to show the performance advantage of the spherical array geometry. The basic geometrical analysis for the spherical arrays has been studied in [45], and characterization of spherical arrays for wireless channels has been studied in [46]. However, construction and analysis of spherical antenna arrays for general mobile communication systems and the corresponding beamforming performance have not been investigated in the literature.

In this paper, we propose the utilization of a uniform spherical array (USA) for future mobile communications, to provide a reliable isotropic beam coverage for all types of user terminals and transmission scenarios. The proposal applies to most of the aforementioned communication scenarios including the IoT wireless connection, aerial mobile links, small cell indoor radio units, and users with wide vertical movements. We provide the performance analysis results in various aspects to demonstrate the effectiveness of the proposed methods, and compare the results to those for conventional arrays. Determination of array parameters, corresponding beam characteristics, and multi-rank transmission performance are presented to confirm the flexibility and usefulness of using USAs for the uniform beam generation to all directions. The array construction based on geodesic partitioning is general enough to include a desired number of antenna elements appropriate for the target beam gain as well as the number of simultaneously supported users. In particular, the basis codebook for spherical arrays is specified and its multi-rank transmission performance is evaluated. The array size which minimizes the inter-beam interference is chosen to provide increased sum-rate performance. The presented codebook can play a similar role to the codebook adopted by the current 5G NR standard, which is based on the discrete Fourier transform (DFT) matrix [24].

The paper is organized as follows. In Section II, geometrical characteristics of USAs are discussed and spherical coordinates of the antenna elements are given. The signal model and beam characteristics are discussed in Section III. Determination of the codebook for USAs and its multi-rank transmission performance are presented in Section IV, followed by the effect of the radiation pattern for each antenna element in Section V. Comparisons with conventional arrays such as the UPA and UCA are made and the results are presented in Section VI. Conclusions are given in Section VII.

II. UNIFORM SPHERICAL ARRAYS

USAs can be constructed using geodesic polyhedra obtained by partitioning edges of a regular polyhedron. Five different regular polyhedra can be used and generation details for geodesic polyhedra can be found in [47]. Although any polyhedra can be used for the array generation, we illustrate the generation procedure using the icosahedron as the basis polyhedron for partitioning. Each edge of the icosahedron is divided into n segments, where n is called the *partition factor*. The division points are mutually connected and each face of the icosahedron is divided into n^2 equilateral triangles of the same size. New crossing points of the connected

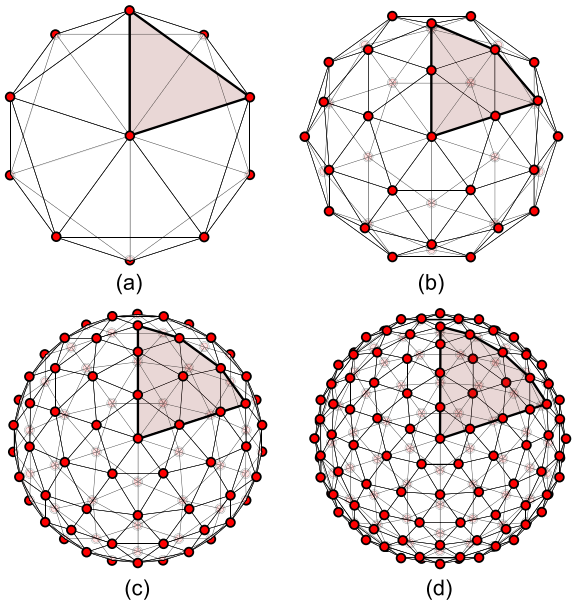

FIGURE 1. Uniform spherical arrays with increasing numbers of antenna elements (a) $M = 12$, (b) $M = 42$, (c) $M = 92$, and (d) $M = 162$.

TABLE 1. Numbers of vertices and faces of geodesic polyhedra with partition factor n.

Polyhedra	$n=1$		$n=2$		$n=3$		$n=4$	
	v	f	v	f	v	f	v	f
Tetrahedron	4	4	10	16	20	36	34	64
Cube	8	6	26	24	56	54	98	96
Octahedron	6	8	18	32	38	72	66	128
Dodecahedron	20	12	32	60	122	240	272	540
Icosahedron	12	20	42	80	92	180	162	320

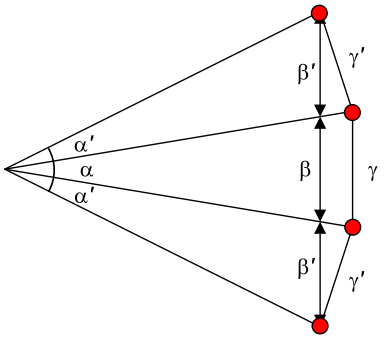

FIGURE 2. Generation of a geodesic polyhedron using partition factor $n = 3$.

lines are projected to the outer sphere of the icosahedron, to form the geodesic polyhedra as shown in Fig. 1, where the shaded area indicates a face of the basis icosahedron. By locating an antenna element at each vertex of the generated geodesic polyhedron, we obtain spherical arrays with M antenna elements. As shown in the figure, the number of antenna elements in red circles is $M = 12$, 42, 92, and 162 for partition factors $n = 1$, 2, 3, and 4, respectively. Fig. 1 suggests that by increasing the number of antenna elements, spatial sampling of the antenna elements on the same sphere increases. However, the radius of the sphere can also be adjusted such that the overall array size as well as the spacing between adjacent antenna elements are determined to produce a desirable beamforming performance. We discuss this issue by introducing the *normalized antenna spacing* in Section IV where the beamforming characteristics for varying geometric parameters are analyzed.

Table 1 shows the numbers of vertices and faces of the resulting geodesic polyhedra with partition factor n, where v denotes the number of vertices and f denotes the number of faces. A number of spherical arrays can be constructed using different basis polyhedra and partition factors, by placing the antenna element at each vertex (or at the center of the face if desired). As the table suggests, the corresponding arrays contain up to hundreds of antenna elements and are well suited for massive MIMO transmission. As the number of faces of the basis polyhedron increases, the uniformity of the resulting array tends to increase and more antenna elements can be placed to the resulting geodesic polyhedron. For these reasons, the remainder discussion is based on icosahedron unless otherwise stated. The result can be extended to arrays based on other polyhedra.

In the conventional method of geodesic polyhedron construction, each edge of the basis regular polyhedron is divided into n equal-length segments, i.e., $\beta = \beta'$ in Fig. 2 which illustrates the partition of an edge with $n = 3$. Upon the projection of the splitting points onto a sphere, most of the triangles on the spherical surface are no longer equilateral triangles. Instead, the arrays can be constructed to have the equal length segments *after* the projection to satisfy $\gamma = \gamma'$ (i.e., $\alpha = \alpha'$) in Fig. 2. Also, geodesic polyhedra with partition factor n can be generated by repeated partitioning using the prime factors of n for higher uniformity, if n can be factored. For example, the spherical array with $M = 162$ elements and partition factor $n = 4$ is generated by two repeated partitioning using $n = 2$. The arrays shown in Fig. 1 have been constructed by applying the aforementioned variations for higher uniformity, leading to beams with regular shapes when beamforming is performed.

The antenna locations in the constructed arrays can be specified by using the spherical coordinate in the 3D space. As shown in Fig. 3, the center of the spherical array is located at O, the origin of spherical coordinate system. Let A_m denote the m-th antenna element located at each vertex of the geodesic polyhedron with zenith angle θ_m and azimuth angle ϕ_m for $m = 1, 2 \ldots, M$. The distance between the array center and the antenna element is denoted by r_m, thus (r_m, θ_m, ϕ_m) represents the spherical coordinate for A_m. Inspection of the arrays shows that all antenna elements, excluding A_1 with $\theta_1 = 0$ and A_M with $\theta_M = \pi$, can be grouped as non-overlapping sets of 5 elements with the same zenith angle. Furthermore, the azimuth angles of the 5 antenna elements in the same group are evenly spaced with the minimum separation of $2\pi/5$. Thus the number of groups is determined as $P = (M-2)/5$ where $M-2$ denotes the number of all antenna elements excluding A_1 and A_M. Group index p is given by $p = \lceil (m-1)/5 \rceil$ for $m = 2, \ldots, M-1$

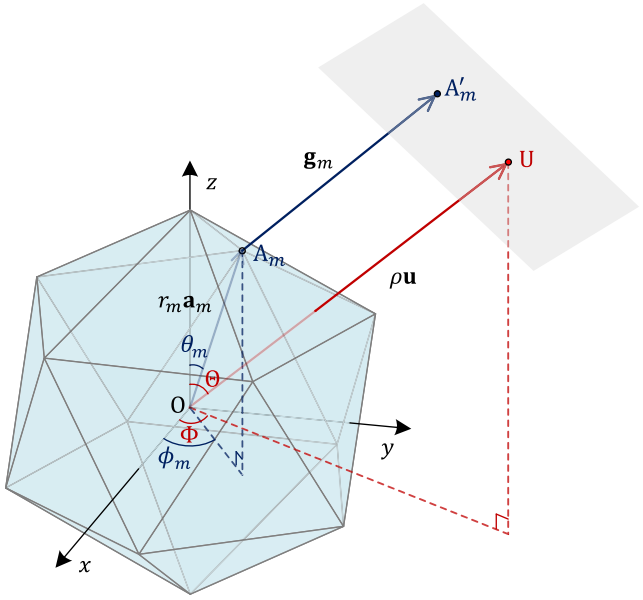

FIGURE 3. Geometric parameters for the spherical array.

where $\lceil x \rceil$ is the ceiling operator denoting the smallest integer no less than x. The distance from the center is the radius of the sphere and common for all antenna elements, i.e., $r_m = r$. We can then specify the coordinate (r, θ_m, ϕ_m) of all antenna elements by presenting zenith angle

$$\theta_m = \begin{cases} 0, & m = 1 \\ \theta'_{\lceil \frac{m-1}{5} \rceil}, & 1 < m \le \dfrac{M}{2} \\ \pi - \theta_{M-m+1}, & \dfrac{M}{2} < m \le M \end{cases} \tag{1}$$

and azimuth angle

$$\phi_m = \begin{cases} 0, & m = 1 \\ \phi'_{\lceil \frac{m-1}{5} \rceil} + \dfrac{2\pi}{5} \times (m \mod 5), & 1 < m \le \dfrac{M}{2} \\ \dfrac{\pi}{5} + \phi_{M-m+1}, & \dfrac{M}{2} < m \le M \end{cases} \tag{2}$$

where θ'_p and ϕ'_p are respectively the group zenith angle and the group azimuth angle offset for $p = \lceil (m-1)/5 \rceil = 1, \ldots, P$. These values are tabularized for partition factors $n = 1, 2, 3$ and 4 in Table 2, which can be used for the array construction and determination of beamforming vectors.

Let U denote the target user for beam transmission, with spherical coordinate (ρ, Θ, Φ), where ρ represents the distance from the center of the array to the user. The vector from O to U is then given by $\rho\mathbf{u}$, where

$$\mathbf{u} = [\, \cos\Phi \sin\Theta \quad \sin\Phi \sin\Theta \quad \cos\Theta \,] \tag{3}$$

is the unit directional vector to the user from the array. Also, let $\mathbf{g}_m$ denote the vector from the m-th antenna element A_m to the user plane, which is the plane perpendicular to $\mathbf{u}$. As shown in Fig. 3, the arrival point of the vector from A_m to the user plane is denoted by A'_m. The vector from O to A_m is represented by $r\mathbf{a}_m$, where

$$\mathbf{a}_m = [\, \cos\phi_m \sin\theta_m \quad \sin\phi_m \sin\theta_m \quad \cos\theta_m \,] \tag{4}$$

TABLE 2. Antenna location parameters for uniform spherical arrays (θ'_p and ϕ'_p are in degrees).

n	p	θ'_p	ϕ'_p	n	p	θ'_p	ϕ'_p
1	1	63.43	0.00	4	1	15.86	0.00
2	1	31.72	0.00		2	26.58	36.00
	2	58.28	36.00		3	31.72	0.00
	3	63.43	0.00		4	43.65	22.39
	4	90.00	18.00		5	43.65	49.61
3	1	21.14	0.00		6	47.58	0.00
	2	37.38	36.00		7	58.28	36.00
	3	42.29	0.00		8	59.62	17.53
	4	58.88	23.62		9	59.62	54.47
	5	58.88	48.38		10	63.43	0.00
	6	63.43	0.00		11	73.95	26.27
	7	79.19	36.00		12	73.95	45.73
	8	81.02	12.40		13	76.56	9.51
					14	76.56	62.49
					15	90.00	18.00
					16	90.00	36.00

is the unit directional vector to the m-th antenna element. Now we define the relative distance $d_m(\Theta, \Phi)$ as

$$d_m(\Theta, \Phi) = |\mathbf{g}_m| - |\rho\mathbf{u}| \tag{5}$$

which is the distance of the beam vector from A_m to the user, subtracted by the distance from the array center to the user. By using the array center as the reference point, $d_m(\Theta, \Phi)$ conveniently represents the relative distance from each antenna element to the user. From the vector geometry observed in Fig. 3, this quantity is identical to the negative dot product between two vectors $\mathbf{u}$ and $r_m\mathbf{a}_m$ which is expressed as

$$\begin{aligned} d_m(\Theta, \Phi) &= -r\, \mathbf{a_m} \cdot \mathbf{u} \\ &= -r\, [\, \cos\phi_m \sin\theta_m \quad \sin\phi_m \sin\theta_m \quad \cos\theta_m \,] \\ &\quad \cdot [\, \cos\Phi \sin\Theta \quad \sin\Phi \sin\Theta \quad \cos\Theta \,]. \end{aligned}$$

Thus we obtain

$$d_m(\Theta, \Phi) = -r\, \{\sin\Theta \sin\theta_m \cos(\Phi - \phi_m) + \cos\Theta \cos\theta_m\}. \tag{6}$$

Combining (6) with the antenna coordinate parameters given by (1) and (2), the exact path difference from each antenna to the user can be computed.

III. BEAMFORMING USING SPHERICAL ARRAYS

The signal transmitted from the antenna array with M elements to K single-antenna users can be written as

$$\mathbf{y} = \mathbf{HWs} + \mathbf{n} \tag{7}$$

where $\mathbf{y} = [y_1\ y_2\ \cdots\ y_K]^T$ is the received signal vector and $\mathbf{H} = [\mathbf{h}_1^T\ \mathbf{h}_2^T\ \cdots\ \mathbf{h}_K^T]^T$ is the $K \times M$ channel matrix with $\mathbf{h}_k = [h_{k,1}\ h_{k,2}\ \cdots\ h_{k,M}]$ denoting the channel vector for the k-th user at $(\rho_k, \Theta_k, \Phi_k)$. The transmitted data vector is denoted by $\mathbf{s} = [s_1\ s_2\ \cdots\ s_K]^T$ and precoding matrix $\mathbf{W} = [\mathbf{w}_1\ \mathbf{w}_2\ \cdots\ \mathbf{w}_K]$ includes beamforming vector for

the k-th user $\mathbf{w}_k = [w_{k,1}\ w_{k,2}\ \cdots\ w_{k,M}]^T$. Vector $\mathbf{n} = [n_1\ n_2\ \cdots\ n_K]^T$ includes the Gaussian noise n_k with power σ^2 for the k-th user.

Assuming only the LoS component exists in the transmission channel with the normalized path loss of 0dB, channel vector $\mathbf{h}_k$ can be represented as $\mathbf{h}_k = \mathbf{b}_k \Lambda_k$, where $\mathbf{b}_k$ and Λ_k are the array response vector and the antenna gain pattern matrix, respectively. Using the distance formula in (6), the $1 \times M$ array response vector is determined as

$$\mathbf{b}_k = [\ e^{j\frac{2\pi}{\lambda}d_1(\Theta_k,\Phi_k)}\ e^{j\frac{2\pi}{\lambda}d_2(\Theta_k,\Phi_k)}\ \cdots\ e^{j\frac{2\pi}{\lambda}d_M(\Theta_k,\Phi_k)}\ ] \quad (8)$$

where λ denotes the carrier wavelength, and the $M \times M$ antenna gain pattern matrix is given by

$$\Lambda_k = \mathrm{diag}[\ \Lambda_{k,1}\ \Lambda_{k,2}\ \cdots\ \Lambda_{k,M}\ ] \quad (9)$$

where $\Lambda_{k,m}$ indicates the radiation attenuation of the m-th antenna elements to the direction of the k-th user. Under the assumption of the ideal isotropic radiation pattern for each antenna element, we have $\Lambda_{k,1} = 1$ for all k and Λ_k becomes the identity matrix. In practical situations, we can apply the gain pattern following the 3GPP model in [48]

$$\Lambda_{k,m} = -\min\left\{12\left(\frac{\varphi_{k,m}}{B_{3dB}}\right)^2,\ 30\right\}\ \mathrm{dB} \quad (10)$$

where B_{3dB} is the 3dB beamwidth and $\varphi_{k,m}$ is an angle between m-th antenna element's boresight and the user direction. It can be determined as

$$\varphi_{k,m} = \cos^{-1}(\mathbf{a}_m \cdot \mathbf{u}_k) \quad (11)$$

where $\mathbf{u}_k = [\ \cos\Phi_k \sin\Theta_k \quad \sin\Phi_k \sin\Theta_k \quad \cos\Theta_k\ ]$. The direction beamforming vector for the k-th user is chosen as the Hermitian of $\mathbf{b}_k$, written as

$$\begin{aligned}\mathbf{w}_k &= \mathbf{b}_k^H \\ &= [\ e^{-j\frac{2\pi}{\lambda}d_1(\Theta_k,\Phi_k)}\ \cdots\ e^{-j\frac{2\pi}{\lambda}d_M(\Theta_k,\Phi_k)}\ ]^T. \end{aligned} \quad (12)$$

For simultaneous beam transmission to K users, the normalization factor of $1/\sqrt{K}$ can be multiplied to (12) to maintain the unit transmission power from each antenna element. Please note that no specific boresight exists for the isotropic source. When we apply the pattern in (10), the antenna boresight is aligned to the direction of the vector from the origin to the antenna element.

The uniform beam characteristics of USAs can be confirmed by generating a pair of users in random directions over the 3D space and evaluating their mutual interference levels. The interference between two beamforming vectors $\mathbf{w}_i$ and $\mathbf{w}_j$ is defined as

$$I_{i,j} = \frac{1}{M}\left|\mathbf{w}_i^H \mathbf{w}_j\right|^2 \quad (13)$$

which is the power of their mutual correlation. The maximum interference level is set to 0dB when two vectors are identical, with the normalization factor $1/M$ in (13). The interference between two beamforming vectors is repeatedly evaluated for two users randomly placed in the 3D space, and the average beam interference is obtained as a function of the angle difference Ψ between two vectors. Fig. 4 shows such evaluation results for the USA based on icosahedron with partition factors $n = 1, 2, 3$, and 4. It can be observed in the figure that beam patterns remain remarkably uniform for any target beam directions over the entire space for all USAs in consideration. It is also noted from the figure that more frequent null locations occur in the beam pattern as the number of antenna elements increases. Such null locations can be exploited to generate multiple beams with very small mutual interference levels. Similar observations can be also be found for the proposed USAs based on other polyhedra. Fig. 5 shows the evaluation results for the mutual interference using the USA based on the dodecahedron with partition factors $n = 1, 2, 3$, and 4.

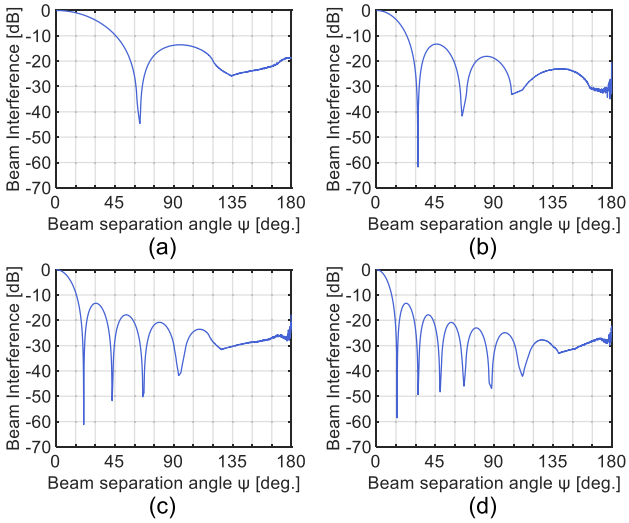

FIGURE 4. Interference between two beamforming vectors for the icosahedron-based arrays: (a) $n = 1$, (b) $n = 2$, (c) $n = 3$, (d) $n = 4$.

The antenna elements in this section are isotropic sources and no consideration has been given to their radiation pattern and polarization, as well as the expected sidelobes levels and the front-to-back ratio. Therefore the sidelobes levels in Figures 4 and 5 are due to the side lobes of the spherical arrays. The beam pattern become different for actual antenna elements with specific radiation patterns, and such an effect is described in Section V.

IV. MULTI-RANK CODEBOOK

As can be observed from the beam characteristics discussed in the previous section, the nulls of the beam power pattern are located at fixed distances from the target direction. If other beams are transmitted to directions corresponding to these null locations, multi-rank beamforming can be performed with a very small amount of mutual interference. Therefore it is a good design attempt to align the directions of codevectors with the locations of the nulls. At the same time, it is desired that a set of codevectors are chosen to cover the entire 3D space in a regular and uniform fashion. These two conditions may not coincide, i.e., regularly spaced beams are not necessarily located at null positions from other beams.

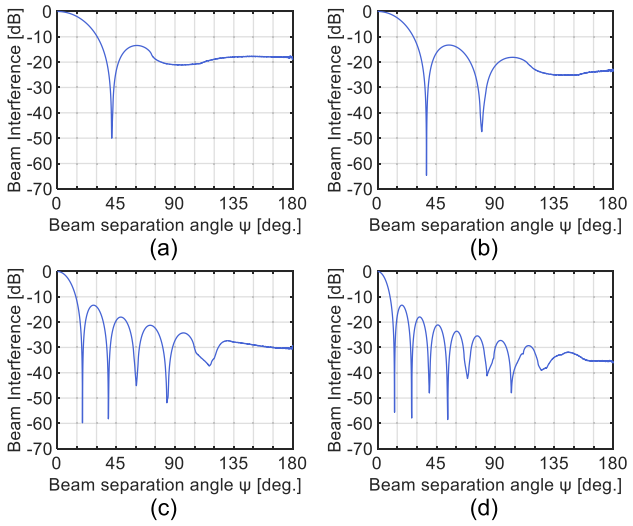

FIGURE 5. Interference between two beamforming vectors for the dodecahedron-based arrays: (a) $n = 1$, (b) $n = 2$, (c) $n = 3$, (d) $n = 4$.

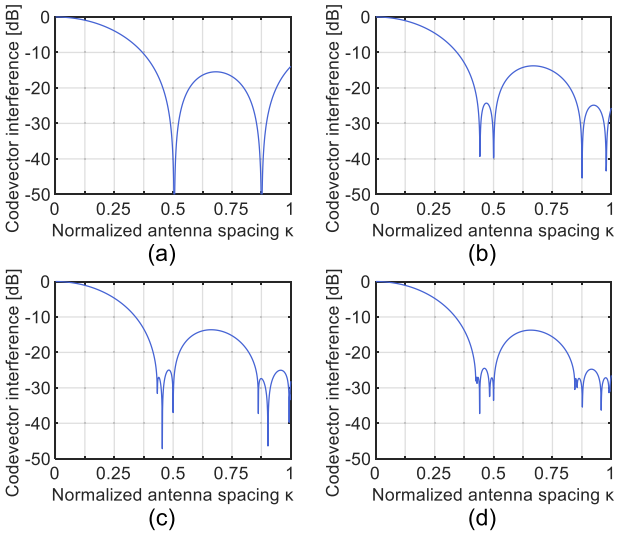

FIGURE 6. Interference between adjacent codevectors for the icosahedron-based arrays with varying antenna spacing: (a) $n = 1$, (b) $n = 2$, (c) $n = 3$, and (d) $n = 4$.

Our design strategy for the determination of basis codevectors is to first align a codevector to the boresight direction of each antenna element, then adjust the physical size of the array such that the selected codevectors exhibit a negligible amount of mutual interference. Hence for the spherical array of M antenna elements, proposed codebook $\mathbf{V}$ consisting of M codevectors is defined as

$$\mathbf{V} = \{\, \mathbf{v}_1,\ \mathbf{v}_2,\ \ldots\ \mathbf{v}_M \,\} \tag{14}$$

where $\mathbf{v}_m$ is the codevector to transmit the beam to the boresight direction of the m-th antenna for $m = 1, 2, \ldots, M$. Codevector $\mathbf{v}_m$ can be determined by substituting $\Theta_k = \theta_m$ and $\Phi_k = \phi_m$ in the expression of the beamforming vector in (12) as

$$\mathbf{v}_m = [\, e^{-j\frac{2\pi}{\lambda}d_1(\theta_m,\phi_m)}\ e^{-j\frac{2\pi}{\lambda}d_2(\theta_m,\phi_m)}\ \ldots\ e^{-j\frac{2\pi}{\lambda}d_M(\theta_m,\phi_m)}\ ]^T. \tag{15}$$

Now we adjust the physical size of the array structure and see the resulting effects on beamforming performance. As we vary the radius r of the spherical array, the distance between neighboring antenna elements also changes. We define the normalized antenna spacing $\kappa = \delta/\lambda$ as the minimum spacing between two adjacent antenna elements divided by the carrier wavelength. Fig. 6 shows the amount of interference versus normalized antenna spacing, for which the average correlation between all pairs of adjacent codevectors are computed for different values of κ. The interference is computed using (13). As indicated by the figure, the first local minimum occurs at $\kappa = 0.5$ for $n = 1$ and significant reduction of interference achieved at $\kappa = 0.44, 0.5$ for $n = 2$. Interference nulling also occurs at $\kappa = 0.43, 0.45, 0.5$ for $n = 3$ and at $\kappa = 0.44, 0.48, 0.5$ for $n = 4$. For all of these κ values, the average interference among adjacent codevectors of -30dB or below is achieved. Choosing $\kappa = 0.5$ results in a significant interference reduction for all partition factors considered, thus we conclude the half-wavelengths spacing between antenna elements works well with the proposed spherical arrays. For this reason, the remainder of analyses is based on half-wavelength spacing between the adjacent elements, although variations on κ can be applied for different partition factors as suggested in Fig. 6. In addition, the antenna elements are all in phase and fed by equal excitation level. The impact on the performance by changing the power level of each antenna element is further discussed in Section V. Please note that antenna coupling may occur as the inter-element spacing reduces significantly below the half-wavelength, and a care has to taken to avoid such undesirable effects and to maintain the beamforming performance.

Simulation was conducted to evaluate the signal-to-interference-plus-noise ratio (SINR) and the sum-rate performance as we increase the transmission rank using the proposed spherical arrays. The noise power was set to satisfy $P/\sigma^2 = 20$dB where P is the received power from each antenna element with the isotropic radiation pattern. We consider K users uniformly distributed over the 3D space, and the channel vector for the k-th user is set as $\mathbf{h}_k = \mathbf{b}_k$ given in (8). For maximum ratio transmission (MRT) without using quantized codevectors, the beamforming vector is chosen as $\mathbf{w}_k = \mathbf{h}_k^H$ and the corresponding SINR for the k-th user becomes

$$\Gamma_k = \frac{\mathbf{h}_k \mathbf{h}_k^H}{\sum_{j\neq k} \mathbf{h}_k \mathbf{h}_j^H}. \tag{16}$$

When using the codebook in (14), the beamforming vector for the k-th user is chosen as $\mathbf{w}_k = \mathbf{v}_{n_k}$, where

$$n_k = \underset{m}{\text{argmax}}\ \mathbf{h}_k \mathbf{v}_m \tag{17}$$

is the index of the codevector with the maximum correlation to the user channel $\mathbf{h}_k$. The SINR of k-th user in this case is

$$\Gamma_k = \frac{\mathbf{h}_k \mathbf{v}_{n_k}}{\sum_{j\neq k} \mathbf{h}_k \mathbf{v}_{n_j}}. \tag{18}$$

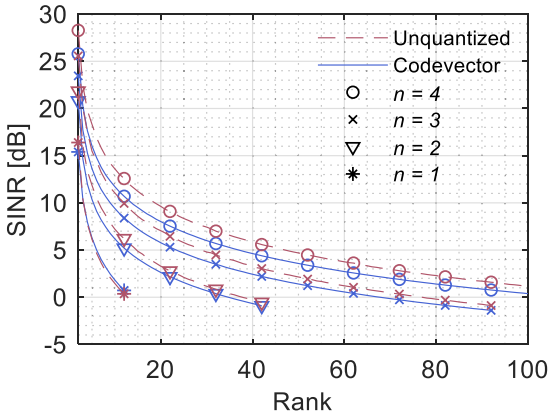

FIGURE 7. SINR versus the transmission rank using icosahedron-based arrays.

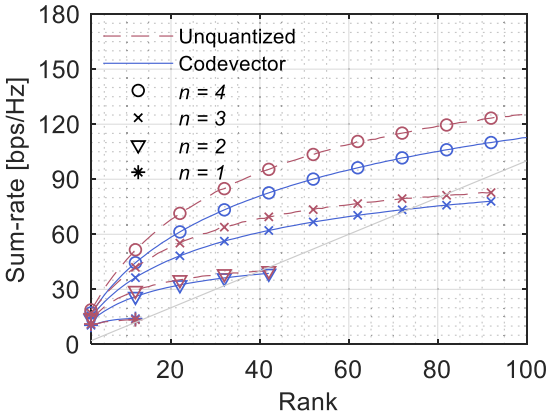

FIGURE 8. Sum-rate versus the transmission rank using icosahedron-based arrays.

For both cases of MRT and codevector transmission, the sum-rate is obtained as

$$R = \sum_{k=1}^{K} \log_2(1 + \Gamma_k). \tag{19}$$

Fig. 7 shows the average SINR values over the entire range of transmission ranks from 1 to M, for four different spherical arrays based on the icosahedron. The solid curves indicate the average SINR achieved by using the proposed codevectors, whereas the dotted curves are for MRT (indicated as 'unquantized' in the figure). Although the SINR decreases as the transmission rank increases, up to full-rank transmission is possible by simultaneously serving M users. It can be confirmed from the figure that only a small amount of degradation occurs by using the quantized codebook requiring $\log_2 M$ bit feedback for the codevector selection, compared to the infinite resolution MRT beamforming. Also, the utilization of larger arrays provide not only increases the rank but enhances the received signal quality. In Fig. 8, the average sum-rate is evaluated and plotted versus the transmission rank. Despite the decreasing SINR observed in Fig. 7, the overall system throughput increases by performing multi-rank transmission with more users. The sum-rate achieved by the quantized codevectors is comparable to the performance obtained by beams with infinite resolution.

V. EFFECTS OF ANTENNA GAINS

Evaluation results in earlier sections are based on the assumption that each antenna element has the isotropic radiation pattern. In order to understand the effect of antenna gains, we apply the radiation pattern in (10) to each antenna element of the spherical array and analyze the resulting transmission performance. The 3dB beamwidth specified in [48] is $B_{3dB} = 65°$. Since the boresights for antenna elements of the spherical array are pointing different directions, one might consider using antenna elements with a wider radiation pattern for improved beamforming performance. The antenna structure becomes more sophisticated for a narrower beamwidth element, thus the identification of an appropriate value of the beamwidth becomes important for both performance and economic perspectives.

We increase the 3dB beamwidth in steps of 30° starting from 65° to apply $B_{3dB} = 65°, 95°, 125°$ and 155° to (10), and plot the resulting beam power patterns in Fig. 9(a). All evaluation results in this section is obtained by using the icosahedron-based array with partition factor $n = 3$. The figure indicates how the beam power is distributed as the separation angle deviates from the target direction. As the 3dB beamwidth decreases, the power contributions from antenna elements located farther away from the target direction also decreases to result in a reduced maximum power level. Fig. 9(b) is obtained by shifting the curves in Fig. 9(a) upwards such that the maximum power value is aligned at 0dB. This version of the figure provides a better indication of relative power levels of the sidelobes, showing that sidelobe power tends to increase for smaller 3dB beamwidth values.

It is also observed in the figure that slight variations occur in null point locations as the beamwidth changes. In order to investigate whether these variations affect the desired spacing between adjacent antenna elements, we evaluate the inter-codevector interference as a function of κ, the antenna spacing δ divided by the wavelength λ. Fig. 10 shows the resulting effect of the spacing in terms of the wavelength on beamforming performance. Despite the increased interference level to approximately -20dB for non-isotropic radiation patterns, $\kappa = 0.5$ still achieves the near-optimal interference reduction between adjacent codevectors for all 3dB beamwidth values in consideration.

Due to the fact that boresight directions of antenna elements in the spherical array are distributed over the 3D space, the contribution of each element to the target beam may become limited if the radiation pattern is non-isotropic. Thus beams can be generated by a subset of antenna elements without significant reduction in beamforming gain. Moreover, unused elements contribute in decreasing the interference to beams in other directions in case of multi-user transmission. Therefore, an optimal number of antenna elements can be found to maximize the sum-rate performance for a given number of simultaneously transmitted beams and the radiation pattern. To investigate this issue, we let only a restricted set of antenna elements to participate in beam-

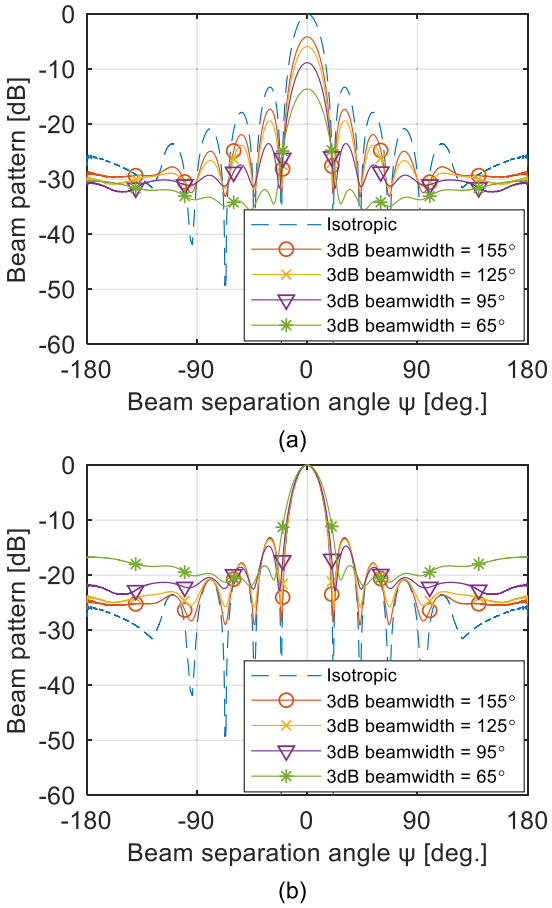

FIGURE 9. Beam characteristics with antenna radiation pattern applied: (a) Varying maximum power, (b) normalized maximum power.

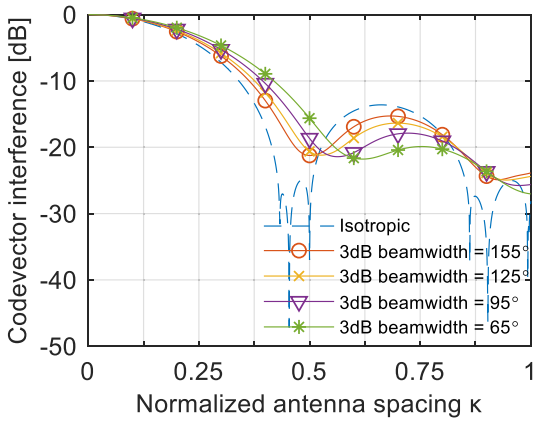

FIGURE 10. Interference between adjacent codevectors for varying antenna spacing with radiation pattern applied.

forming and observe the resulting performance. The restriction range is determined by the angle from the codevector direction. Beginning from the single antenna element pointing the codevector direction, we progressively include more elements which are within angles θ_1, $2\theta_1$, $3\theta_1$, …, where θ_1 is the first group zenith angle defined in (1) and Table 1. Including the elements within $5\theta_1$ corresponds to using half of all antenna elements for beamforming. Fig. 11 shows

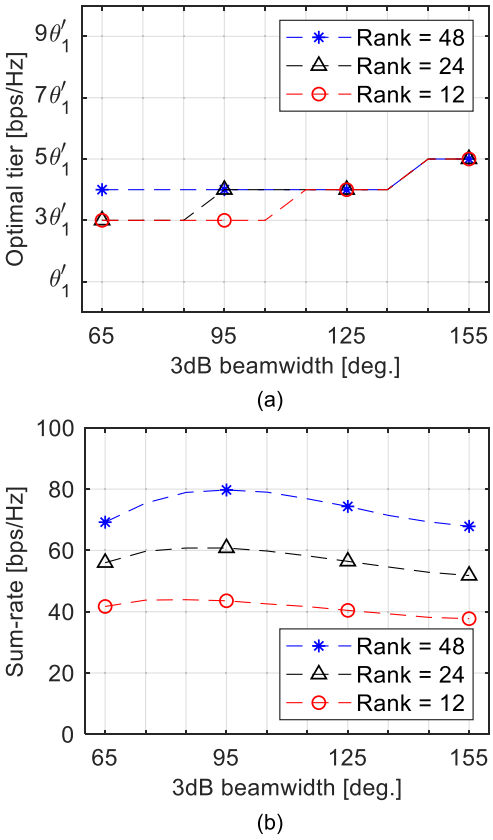

FIGURE 11. Sum-rate versus the 3dB beamwidth: (a) Optimal restriction angle for antenna elements participating in beamforming, (b) the corresponding maximum sum-rate.

the restriction angle resulting in the maximum sum-rate and the corresponding sum-rate for different 3dB beamwidths. As can be seen from the figure, the restriction angle which produces the maximum sum-rate (indicated by *optimal tier* in Fig. 11(a)) lie in the vicinity of $4\theta_1$. Therefore, utilizing less than half of all antenna elements suffices to achieve the desirable transmission performance. Inclusion of more elements reduces the sum-rate due to the mutual interference. Fig. 11(b) further indicates that the 3dB beamwidth of 95° maximizes the sum-rate. A wider radiation pattern not only increases the target beam gain but also the interference to other users, diminishing the overall transmission performance. For this evaluation, 12, 24 and 48 random users are generated in the 3D space and the codebook in Section IV is used for beamforming.

VI. PERFORMANCE COMPARISON

The performance of the proposed spherical arrays is compared to existing conventional arrays in this section. The first comparison is regarding the uniformity of the beam pattern including the null locations. The zenith angle of the beam direction is illustrated in Fig. 12. The beam power pattern is evaluated by applying the beamforming vector in (12) to the icosahedron-based USA with partition factor $n = 3$, and the resulting patterns are shown in Fig. 13(a). The minimum spacing δ between two adjacent antenna elements is set to be half wavelengths, i.e., $\delta = \lambda/2$. The beams are generated in

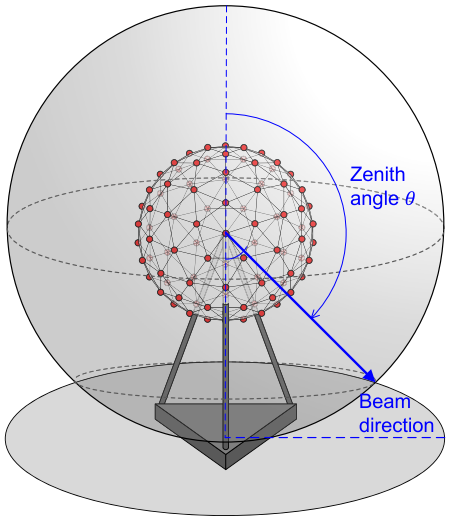

FIGURE 12. Three-dimensional beam direction from the spherical array.

four different target directions of $\theta = 0°, 10°, 20°$ and $30°$. It is observed from the figure that the beam patterns for different target directions are shifted versions of one another, with no change in their general shapes. Regardless of the target directions, the beam pattern stays the same without any distortion and the beam uniformity is maintained. For all beam patterns in the figure, the first null points from the peak are located at $\theta = \pm 21°$ with power level -53dB, and the second null points are at $\theta = \pm 43°$ with power level -70dB. Note that null points occur at symmetric distances from the peak with very low signal power. While the null points occur at roughly integer multiples of $21°$, such characteristics disappear after the fourth null points.

The relative null locations from the peak are further evaluated for varying target beam directions from $0°$ to $60°$ as shown in Fig. 13(b). Constant values of $\pm 21°$ and $\pm 43°$ are maintained for the entire range of beam directions, indicated by solid lines in the figure. Such uniformity of beam patterns cannot be found for the UPA tested for comparison. The dotted lines in Fig. 13(b) indicate the relative null locations from the peak for the UPA with $M = 32$ elements, a 4-by-8 two-dimensional array with half-wavelengths spacing between adjacent elements. Although the beam patterns remain relatively symmetric for beam directions near $\theta = 0°$, distortion begins to occur as θ increases. Significant amounts of asymmetry occurs for null locations when $\theta > 30°$.

The UPA also suffers the loss of the peak power when the beam direction deviates from the array boresight due to the radiation pattern of antenna elements. On the other hand, USAs exhibit a distinctive advantage over the conventional arrays by providing stable and uniform beam power patterns in all target directions. The uniformity of the beam pattern for the spherical arrays can be further confirmed by comparing the beam interference pattern in Fig. 4 with that of the UPA. Fig. 14 shows that an identical beam interference pattern is formed for spherical arrays with clear null locations for any pair of beamforming vectors in two random directions. The

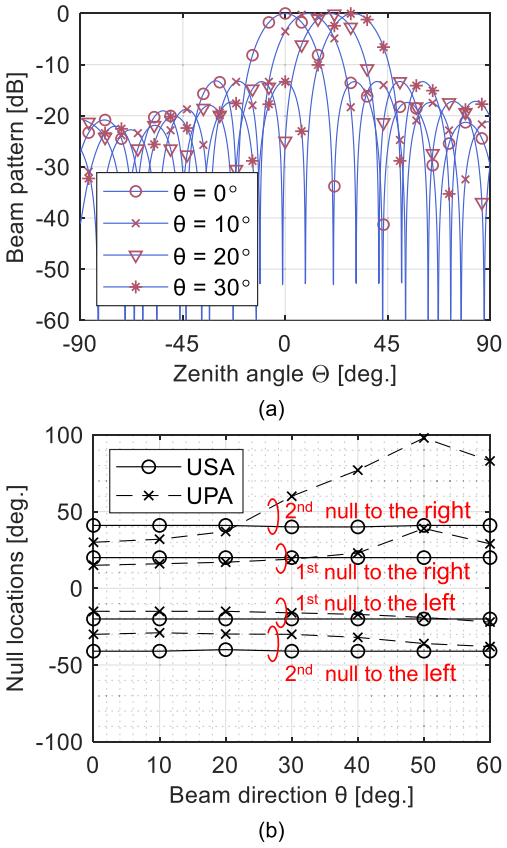

FIGURE 13. Beam characteristics for different target directions: (a) Beam pattern, (b) null point locations.

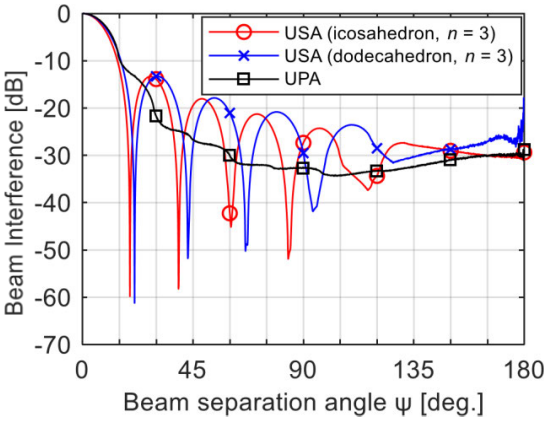

FIGURE 14. Interferences between two beamforming vectors for the spherical arrays and the UPA.

UPA fails to exhibit a beam interference pattern with nulls as shown in the figure, since the beam shape changes for different target directions.

Fig. 15 illustrates the key advantage of using spherical arrays by showing that the received power level stays constant regardless of the user locations. As the user moves from zenith angle θ of $0°$ to $180°$ in Fig. 12, the peak received power becomes maximum at $\theta = 90°$ for the UPA and UCA, i.e., when the target beam direction is parallel to the ground surface. For this power level evaluation, the UPA of 32 elements with 4 horizontal and 8 vertical arrays is

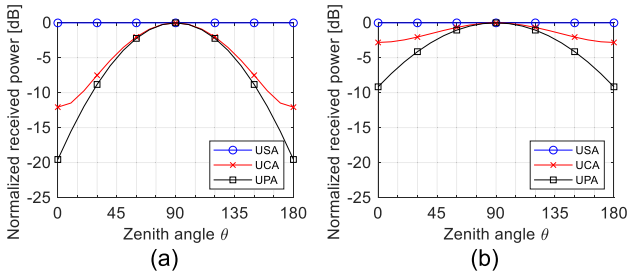

FIGURE 15. Relative received power levels for varying target directions: (a) 3dB beamwidth = 65°, (b) 3dB beamwidth = 95°.

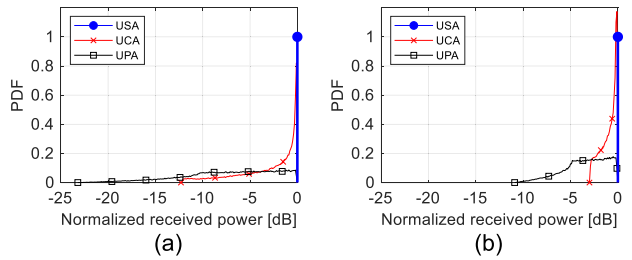

FIGURE 16. Distributions for relative received power levels using different arrays: (a) 3dB beamwidth = 65°, (b) 3dB beamwidth = 95°.

assumed, which covers a 120° sector. For three sectors in a cell, three UPAs are used with the total number of antenna elements $M = 96$. For the UCA evaluation, 4 vertical layers of 24-element circular arrays are assumed, with the same total number of antenna elements $M = 96$ to cover the whole cell. The icosahedron-based USA with partition factor $n = 3$ includes $M = 92$ antenna elements. As shown in Fig. 15, the USA exhibits the constant peak power for all target directions from $\theta = 0°$ (upward direction) to $\theta = 180°$ (downward direction), covering the 3D space with the same beam intensity. Note the power level in the figure is normalized to indicate the maximum power as the reference value of 0dB. The power difference experienced by using the UPA and UCA becomes more severe for the smaller 3dB beamwidth as shown in Fig. 15(a), which shows the difference amounts to 20dB for the UPA and 12dB for the UCA. If the 3dB beamwidth is 95°, the difference respectively reduces to 9dB and 3dB as indicated in Fig. 15(b). Such direction-dependent power variation behaviors are shown in the form of the probability density function in Fig. 16, assuming random target directions in the 3D space. The received power levels for conventional arrays are shown to be distributed over a wide range of values, unlike the spherical array providing the identical beam power.

VII. CONCLUSION

Construction of spherical arrays based on geodesic polyhedra is described and corresponding beam characteristics are presented, to demonstrate the advantage of using such arrays for all-directional beamforming. The codebook supporting up to the full-rank data transmission is proposed, with a negligible inter-beam interference achieved by conventional half-wavelengths spacing between adjacent antenna elements.

The presented parameters and performance evaluation results can be used to choose appropriate design parameters for spherical arrays. Table 2 provides the antenna locations for the arrays with $M = 12$, 42, 92, and 162 antenna elements, and the corresponding normalized antenna spacing can be adjusted using Fig. 6 to minimize the multi-beam interference. Achievable sum-rates using different array sizes and transmission ranks are determined as indicated in Fig. 8. The impact of the 3dB beamwidth on the antenna spacing and the partial usage of the antenna elements is shown in Figures 10 and 11. Simulation results confirm that a partial usage of antenna elements in a hemisphere of the array is sufficient to provide the desirable throughput performance, with the 95° 3dB beamwidth radiation pattern.

REFERENCES

[1] Z. Zhang, Y. Xiao, Z. Ma, M. Xiao, Z. Ding, X. Lei, G. K. Karagiannidis, and P. Fan, "6G wireless networks: Vision, requirements, architecture, and key technologies," *IEEE Veh. Technol. Mag.*, vol. 14, no. 3, pp. 28–41, Sep. 2019.

[2] T. S. Rappaport, Y. Xing, O. Kanhere, S. Ju, A. Madanayake, S. Mandal, A. Alkhateeb, and G. C. Trichopoulos, "Wireless communications and applications above 100 GHz: Opportunities and challenges for 6G and beyond," *IEEE Access*, vol. 7, pp. 78729–78757, 2019.

[3] P. Yang, Y. Xiao, M. Xiao, and S. Li, "6G wireless communications: Vision and potential techniques," *IEEE Netw.*, vol. 33, no. 4, pp. 70–75, Jul. 2019.

[4] M. Xiao, S. Mumtaz, Y. Huang, L. Dai, Y. Li, M. Matthaiou, G. K. Karagiannidis, E. Björnson, K. Yang, and A. Ghosh, "Millimeter wave communications for future mobile networks," *IEEE J. Sel. Areas Commun.*, vol. 35, no. 9, pp. 1909–1935, Sep. 2017.

[5] J. G. Andrews, T. Bai, M. N. Kulkarni, R. W. Heath, Jr., A. Alkhateeb, and A. K. Gupta, "Modeling and analyzing millimeter wave cellular systems," *IEEE Trans. Commun.*, vol. 65, no. 1, pp. 403–430, Jan. 2017.

[6] I. A. Hemadeh, K. Satyanarayana, M. El-Hajjar, and L. Hanzo, "Millimeter-wave communications: Physical channel models, design considerations, antenna constructions, and link-budget," *IEEE Commun. Surveys Tuts.*, vol. 20, no. 2, pp. 870–913, 2nd Quart., 2018.

[7] A. Shahmansoori, G. E. Garcia, G. Destino, G. Seco-Granados, and H. Wymeersch, "Position and orientation estimation through millimeter-wave MIMO in 5G systems," *IEEE Trans. Wireless Commun.*, vol. 17, no. 3, pp. 1822–1835, Mar. 2018.

[8] R. W. Heath, Jr., T. Shimizu, V. Va, and G. Bansal, "Millimeter wave V2X communications: Use cases and design considerations of beam management," in *Proc. Asia–Pacific Microw. Conf. (APMC)*, Kyoto, Japan, Nov. 2018, pp. 183–185.

[9] G. Naik, B. Choudhury, and J.-M. Park, "IEEE 802.11bd & 5G NR V2X: Evolution of radio access technologies for V2X communications," *IEEE Access*, vol. 7, pp. 70169–70184, 2019.

[10] L. Shan, R. Miura, T. Kagawa, F. Ono, H.-B. Li, and F. Kojima, "Machine learning-based field data analysis and modeling for drone communications," *IEEE Access*, vol. 7, pp. 79127–79135, 2019.

[11] M. Mozaffari, A. Taleb Zadeh Kasgari, W. Saad, M. Bennis, and M. Debbah, "Beyond 5G with UAVs: Foundations of a 3D wireless cellular network," *IEEE Trans. Wireless Commun.*, vol. 18, no. 1, pp. 357–372, Jan. 2019.

[12] Y. Zeng, J. Lyu, and R. Zhang, "Cellular-connected UAV: Potential, challenges, and promising technologies," *IEEE Wireless Commun.*, vol. 26, no. 1, pp. 120–127, Feb. 2019.

[13] J. Zhang, X. Ge, Q. Li, M. Guizani, and Y. Zhang, "5G millimeter-wave antenna array: Design and challenges," *IEEE Wireless Commun.*, vol. 24, no. 2, pp. 106–112, Apr. 2017.

[14] *Evolved Universal Terrestrial Radio Access (EUTRA); Physical Channels and Modulation (Release 10)* document TS 36.211 V10.0.0, 3GPP, Dec. 2010.

[15] *Evolved Universal Terrestrial Radio Access (EUTRA); Physical Layer Procedures (Release 14)*, document TS 36.213 V14.1.0, 3GPP, Dec. 2016.

[16] Q.-U.-A. Nadeem, A. Kammoun, M. Debbah, and M.-S. Alouini, "3D massive MIMO systems: Modeling and performance analysis," *IEEE Trans. Wireless Commun.*, vol. 14, no. 12, pp. 6926–6939, Dec. 2015.

[17] X. Li, S. Jin R. W. Heath, Jr., and X. Gao, "Three-dimensional beamforming for large-scale FD-MIMO systems exploiting statistical channel state information," *IEEE Trans. Veh. Technol.*, vol. 65, no. 11, pp. 8992–9005, Nov. 2016.
[18] S. Shin, H. Lee, C. Kim, W. Sung, and J. Park, "Parameterised codebook design based on channel statistics for efficient multi-rank MIMO transmission," *IET Commun.*, vol. 12, no. 15, pp. 1880–1890, Sep. 2018.
[19] E. Onggosanusi, M. S. Rahman, L. Guo, Y. Kwak, H. Noh, Y. Kim, S. Faxer, M. Harrison, M. Frenne, S. Grant, R. Chen, R. Tamrakar, and A. Q. Gao, "Modular and high-resolution channel state information and beam management for 5G new radio," *IEEE Commun. Mag.*, vol. 56, no. 3, pp. 48–55, Mar. 2018.
[20] I. Ahmed, H. Khammari, A. Shahid, A. Musa, K. S. Kim, E. De Poorter, and I. Moerman, "A survey on hybrid beamforming techniques in 5G: Architecture and system model perspectives," *IEEE Commun. Surveys Tuts.*, vol. 20, no. 4, pp. 3060–3097, 4th Quart., 2018.
[21] H. Seleem, A. I. Sulyman, and A. Alsanie, "Hybrid precoding-beamforming design with Hadamard RF codebook for mmWave large-scale MIMO systems," *IEEE Access*, vol. 5, pp. 6813–6823, 2017.
[22] R. Li, S. He, Y. Huang, Y. Li, and L. Yang, "Analysis of panel antenna arrays in los MIMO system," *IEEE Access*, vol. 6, pp. 23303–23315, 2018.
[23] Y. Huang, Y. Li, H. Ren, J. Lu, and W. Zhang, "Multi-panel MIMO in 5G," *IEEE Commun. Mag.*, vol. 56, no. 3, pp. 56–61, Mar. 2018.
[24] *NR; Physical Layer Procedures for Data (Release 15)*, document TS 38.214 V15.6.0, 3GPP, Jun. 2019.
[25] H. Q. Ngo, E. G. Larsson, and T. L. Marzetta, "The multicell multiuser MIMO uplink with very large antenna arrays and a finite-dimensional channel," *IEEE Trans. Commun.*, vol. 61, no. 6, pp. 2350–2361, Jun. 2013.
[26] K. Huang, J. Chen, and V. K. N. Lau, "Communication using a large-scale array of ubiquitous antennas: A geometry approach," *IEEE Trans. Signal Process.*, vol. 64, no. 14, pp. 3635–3650, Jul. 2016.
[27] E. Y. Menta, K. Ruttik, R. Jäntti, P. Kela, and K. Leppänen, "Modeling and analysis of dynamic pilot scheduling scheme for 5G ultra-dense network," in *Proc. IEEE 5G World Forum (5GWF)*, Silicon Valley, CA, USA, Jul. 2018, pp. 44–48.
[28] J. Song, J. Choi, and D. J. Love, "Common codebook millimeter wave beam design: Designing beams for both sounding and communication with uniform planar arrays," *IEEE Trans. Commun.*, vol. 65, no. 4, pp. 1859–1872, Apr. 2017.
[29] J. Mo, B. L. Ng, S. Chang, P. Huang, M. N. Kulkarni, A. Alammouri, J. C. Zhang, J. Lee, and W.-J. Choi, "Beam codebook design for 5G mmWave terminals," *IEEE Access*, vol. 7, pp. 98387–98404, 2019.
[30] D. Zhu, J. Choi, R. W. Heath, Jr., Q. Cheng, and W. Xiao, "High-resolution angle tracking for mobile wideband millimeter-wave systems with antenna array calibration," *IEEE Trans. Wireless Commun.*, vol. 17, no. 11, pp. 7173–7189, Nov. 2018.
[31] M. Giordani, M. Polese, A. Roy, D. Castor, and M. Zorzi, "A tutorial on beam management for 3GPP NR at mmWave frequencies," *IEEE Commun. Surveys Tuts.*, vol. 21, no. 1, pp. 173–196, 1st Quart., 2019.
[32] M. Giordani, M. Polese, A. Roy, D. Castor, and M. Zorzi, "Standalone and non-standalone beam management for 3GPP NR at mmWaves," *IEEE Commun. Mag.*, vol. 57, no. 4, pp. 123–129, Apr. 2019.
[33] P. Ioannides and C. A. Balanis, "Uniform circular and rectangular arrays for adaptive beamforming applications," *IEEE Antennas Wireless Propag. Lett.*, vol. 4, pp. 351–354, 2005.
[34] L. Wu, H. Yang, and D. Wang, "Hadamard transform based codebook design for uniform circular arrays in mobile radio communications," in *Proc. IEEE VTC-Fall*, Quebec City, QC, Canada, Sep. 2012, pp. 1–5.
[35] T. Thomas and F. Vook, "Improving the performance of the UCA when using LTE codebook feedback," in *Proc. IEEE WCNC*, Shanghai, China, Apr. 2012, pp. 847–851.
[36] A. Koc, A. Masmoudi, and T. Le-Ngoc, "Hybrid beamforming for uniform circular arrays in multi-user massive MIMO systems," in *Proc. IEEE Can. Conf. Electr. Comput. Eng. (CCECE)*, Edmonton, AB, Canada, May 2019, pp. 1–4.
[37] F. Zhang and W. Fan, "Near-field ultra-wideband mmWave channel characterization using successive cancellation beamspace UCA algorithm," *IEEE Trans. Veh. Technol.*, vol. 68, no. 8, pp. 7248–7259, Aug. 2019.
[38] H. Jing, W. Cheng, and X.-G. Xia, "A simple channel independent beamforming scheme with parallel uniform circular array," *IEEE Commun. Lett.*, vol. 23, no. 3, pp. 414–417, Mar. 2019.
[39] T. Liu, C. Zhang, Q. Shi, and X. Zhao, "Array gain analysis of uniform circular array mounted on a cylinder," in *Proc. Int. Conf. Qual., Rel., Risk, Maintenance, Saf. Eng.*, Chengdu, China, Jun. 2012, pp. 1485–1488.
[40] E. Guangxi and H. Yang, "Design and test of geodesic dome phased array system for multi-target TT&C and communication," in *Proc. 15th Int. Conf. Opt. Commun. Netw. (ICOCN)*, Hangzhou, China, Sep. 2016, pp. 1–3.
[41] M. Henderson, M. B. Davis, and M. Huisjen, "GDPAA advanced technology demonstration overview and results," in *Proc. IEEE Int. Symp. Phased Array Syst. Technol.*, Waltham, MA, USA, Oct. 2010, pp. 140–143.
[42] F. Zotter and B. Bank, "Geometric error estimation and compensation in compact spherical loudspeaker array calibration," in *Proc. IEEE Int. Instrum. Meas. Technol. Conf. Proc.*, Graz, Austria, May 2012, pp. 2710–2715.
[43] L. Zhang, "Sound source localization using non-conformal surface sound field transformation based on spherical harmonic wave decomposition," *Sensors*, vol. 17, p. 1087, May 2017.
[44] B. Tomasic, J. Turtle, and S. Liu, "Spherical arrays–design considerations," in *Proc. 18th Int. Conf. Appl. Electromagn. Commun.*, Dubrovnik, Croatia, Dec. 2005, pp. 1–8.
[45] A. Guerra, F. Guidi, and D. Dardari, "Single-anchor localization and orientation performance limits using massive arrays: MIMO vs. Beamforming," *IEEE Trans. Wireless Commun.*, vol. 17, no. 8, pp. 5241–5255, Aug. 2018.
[46] O. Franek and G. F. Pedersen, "Spherical arrays for wireless channel characterization and emulation," in *Proc. IEEE-APS Topical Conf. Antennas Propag. Wireless Commun. (APWC)*, Palm Beach, FL, USA, Aug. 2014, pp. 480–483.
[47] R. Szmit, "Geometry design and structural analysis of steel single-layer geodesic domes," in *Proc. Baltic Geodetic Congr. (BGC Geomatics)*, Gdansk, Poland, 2017, pp. 205–209.
[48] *Evolved Universal Terrestrial Radio Access (EUTRA); Study on Channel Model for Frequencies From 0.5 to 100GHz (Release 15)*, document TR 38.901 V15.0.0, 3GPP, Jun. 2018.

WONJAE RYOO (Student Member, IEEE) received the B.S. degree in electronic engineering from Sogang University, South Korea, in 2018, where he is currently pursuing the M.S. degree in electrical engineering. He is also a Research Assistant with the Digital Transmission Laboratory, Sogang University. He has coauthored multiple academic publications and patents in the area of efficient signal transmission using large-scale arrays. His research interests include massive MIMO, millimeter-wave channel models, and physical layer communications with the aid of machine learning.

WONJIN SUNG (Member, IEEE) received the B.S. degree from Seoul National University, South Korea, in 1990, and the M.S. and Ph.D. degrees in electrical engineering from the University of Michigan, Ann Arbor, MI, USA, in 1992 and 1995, respectively. From January 1996 to August 2000, he worked at Hughes Network Systems, Germantown, MD, USA, where he participated in development projects of cellular and satellite systems, including IS-136 base station modems, multimode ground terminals for medium orbit satellites, and Inmarsat-IV system air interface design. Since September 2000, he has been with the Department of Electronic Engineering, Sogang University, Seoul, South Korea, where he is currently a Professor. From August 2008 to July 2009, he was, on a sabbatical leave, a Visiting Scholar from Arizona State University, Tempe, AZ, USA, analyzing multi-cell cooperative transmission strategies and their impact on cell-edge performance. From 2012 to 2015, he was the project leader and chief investigator to develop the concept of a cognitive radio-based cellular system over an unlicensed spectrum under the sponsorship of IITP, South Korea. He is also the chief investigator for designing next-generation codebooks for 5G NR, sponsored by the National Research Foundation of Korea, since 2017. He holds 70 patents, including 25 U.S. patents in the area of wireless communications. His current research interests include beamforming and reference signaling for massive MIMO, standardization issues for 5G and beyond, millimeter-wave transmission, and spatial channel modeling.